Convergent Rayleigh-Taylor Experiments on the Nova Laser

C. Cherfils,[1] S. G. Glendinning,[2] D. Galmiche,[1] B. A. Remington,[2] A. L. Richard,[1] S. Haan,[2] R. Wallace,[2] N. Dague,[1] and D. H. Kalantar[2]

[1]*CEA-DAM Ile de France, BP 12, 91680 Bruyères le Chatel, France*
[2]*LLNL, P.O. Box 808, Livermore, California 94551*

(Received 22 January 1999)

Experiments have been done on the Nova laser to investigate the effects of convergence on Rayleigh-Taylor growth. We ablatively accelerated planar CH(Br) foils or hemispherical CH(Ge) capsules with identical initial perturbations. Experimental results showed the decrease of the effective wavelength of the perturbation and the early onset of nonlinearity in the converging case compared to the planar case. Numerical simulations using the 2D Lagrangian code FCI2 are in good agreement with the experimental results.

PACS numbers: 52.35.Py, 47.20.–k, 52.40.Nk, 52.70.La

For inertial confinement fusion, the Rayleigh-Taylor (RT) instability is a major constraint. The RT instability occurs mainly at the ablation front during the acceleration phase and at the pusher-fuel interface during the deceleration phase. Growth of perturbations at the capsule outer and inner surfaces due to the RT instability have to be kept under control in order to achieve sufficient hydrodynamic efficiency to reach ignition. Many experiments have measured RT growth in planar geometry and have verified the effect of ablative stabilization [1–5], but few experiments have examined the role of convergence [6–9]. Weir *et al.* [9] measured RT growth in a 2D cylindrically convergent geometry by imploding gelatin cylinders with high-pressure gases. The RT growth was at a classical interface, that is, not at an ablation front. The gelatin was incompressible and stayed in the solid state throughout the experiment, though material strength was thought to be negligible. Hsing *et al.* [8] used the Nova laser to generate a radiation drive to implode cylinders at high compression. They studied RT growth at the ablation front and measured the perturbation feedthrough to an internal marker layer by viewing the imploding cylinders side-on. An early transition to the nonlinear regime was inferred by observing mode coupling to low-order modes seeded by the drive. In spherically convergent geometry, RT growth experiments at the ablation front have been done in direct drive [6,7]; associated diagnostics were side-on and face-on radiographs which suffered from limited spatial and temporal resolutions.

Radiation driven experiments have been conducted on the Nova laser at the Lawrence Livermore National Laboratory in order to study the effect of convergence on the linear and weakly nonlinear growth phase of the RT instability at the ablation front [10–12]. Experiments are performed in both planar and spherical geometry with the perturbation growth diagnosed by face-on radiography. Corrugated spheres or planar foils are mounted on the side of a hohlraum, with 2D sinusoidal perturbations facing the inside of the hohlraum. In the present paper, we report our experimental results of ablation front RT instability in planar and spherically convergent geometry and compare our results with 2D hydrodynamic simulations performed at CEA/DIF using the Lagrangian code FCI2.

The Nova experimental configuration is shown in Fig. 1. A standard Au "scale-1" hohlraum is used (2.75 mm long by 1.6 mm diameter). The experimental sample is a standard "HEP-4" capsule [13] corresponding to a 530 μm outer diameter, 42 μm wall thickness, CH (1.3% Ge) capsule with no fill pressure. This capsule is mounted on a hole in the wall of the hohlraum, with half the sphere interior to the hohlraum, and half exterior. The interior hemisphere has a 70 μm wavelength, 2 μm amplitude, 2D single mode sinusoidal perturbation imposed on it, using an off-line laser ablation technique [14]. For comparison, identical experiments were conducted, using 50 μm thick

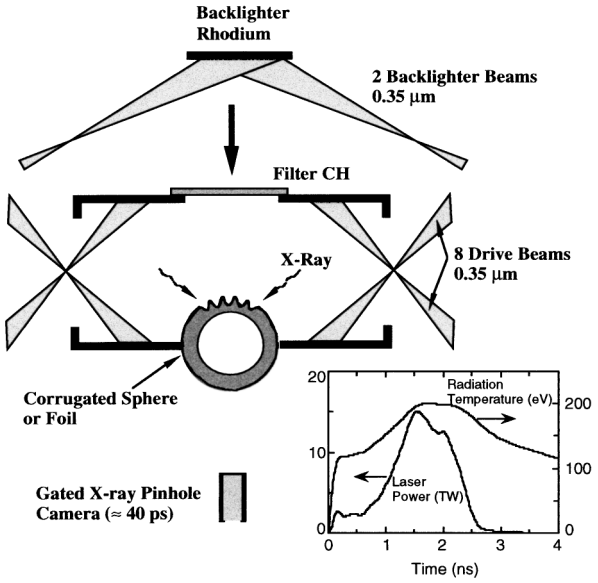

FIG. 1. Experimental setup. Samples are planar foils of CH(Br) or spherical capsules of CH(Ge). Pulse shape PS26 and average drive temperature are plotted at the bottom of the figure.

planar foils of CH(2% Br) in place of the hemispheres. Br dopant was used here, because we were unable to fabricate planar CH(Ge) foils. The Br concentration was adjusted to provide the same degree of x-ray preheat shielding, based on 1D simulations. Eight of the ten Nova beams enter the hohlraum in a 2.2 ns shaped ("PS26"), 6:1 contrast pulse, and convert to x rays. Total input energy is about 20 kJ. Two beams are used to irradiate a rhodium disk to create a 2.7–3.4 keV x-ray backlighting source. A fast x-ray framing camera [15] with a fast high-voltage pulse forming network images the foil or sphere. Time sequences of raw images, taken with this camera run at 8× magnification with 10 μm pinholes at 40 ps gating times, are shown in Fig. 2. The top row corresponds to the planar CH(Br) foil, and the bottom row corresponds to the CH(Ge) hemisphere. The last image for the planar case shows the evolution of the perturbation into the nonlinear regime. For the spherical case, the shrinking of the perturbation patch illustrates the convergence of the capsule by over a factor of 2. Simulating the experimental x-ray radiographs was a multistep process. First, we estimated a mean radiation drive temperature using a 3D view factor code. This code included radiative transport but no hydrodynamics and allowed us to estimate the effect on the x-ray drive of nonaxisymmetric laser beams. On top of the capsule, in the angular range 56°–90° relative to the wall of the hohlraum, peak drive temperature values range between 195 and 201 eV and are quite similar to the peak temperatures obtained with the view factor code for the planar configuration. The average drive temperature we obtained this way is in good agreement with the radiation temperature inferred from Dante measurements [11].

We then used the 2D radiation hydrodynamics code FCI2 to simulate the capsule implosion or foil acceleration and subsequent perturbation development due to the RT instability. FCI2 is a 2D Lagrangian code with rezoning, including nonlocal thermal equilibrium atomic physics, heat conduction with flux limiting, and different radiation transport packages [16]. A multigroup diffusion radiation transport method has been used in our calculations, with a radiation spectral shape extracted from a holhraum simulation assuming cylindrical symmetry [17]. We checked

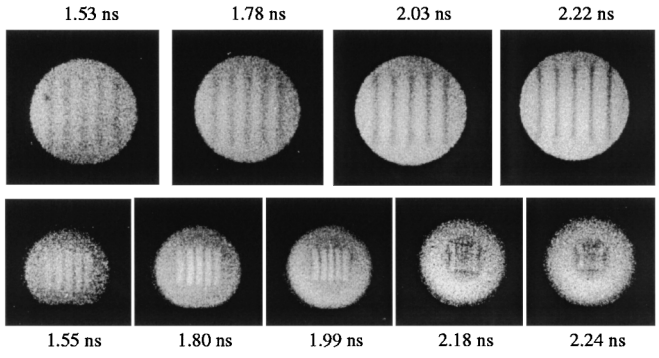

FIG. 2. Raw images comparing planar (top) with spherically convergent (bottom) RT growth.

that FCI2 correctly predicted the mean flow evolution (gross hydrodynamics) in both the planar and spherical cases. In the hemispherical case, an important issue was evaluating whether edge effects perturbed our face-on radiography measurements of the capsule. We have evaluated this concern in two ways. First, we did an FCI2 simulation of the capsule surrounded by an Au washer, approximating locally the cylindrical hohlraum by a planar wall to get an axisymmetric configuration. Vacuum was treated as a very low density, transparent fluid. This simulation shows no disturbance of the region of interest prior to 2.5 ns. This confirms the experimental evidence of a large, nonperturbing diagnostic window in the hohlraum throughout the time interval of interest, $0 \leq t \leq 2.24$ ns. A second way to assess this potential concern is to estimate the time Δt for a disturbance at the Au-CHGe boundary to travel along the capsule to the region of our observations. The simulated isothermal sound speed in the shell near the equator varies from 25 μm/ns ($t = 0$ ns) to 100 μm/ns ($t = 1.7$ ns) and stays fairly constant thereafter. As the distance the sound wave would have to travel is roughly $R_{\text{inner}} \times \pi/3 = 230$ μm, this gives a lower bound of $\Delta t = 3$ ns, which is larger than the duration of the experiment. We conclude that, in the angular range and time interval we are interested in, the edge effects are insignificant, the capsule stays spherical, and the wavelength $\lambda(t)$ stays proportional to the nonperturbed ablation front radius. As shown in Fig. 3, for the planar configuration, FCI2 simulations are in good agreement with the foil trajectory data, and for the perturbed capsule, our simulations reproduce the wavelength evolution. In Fig. 3 are also represented the peak density and the electron temperature at the location of peak density versus time for both the planar and spherical cases. The peak density profiles show that shock breakout on the rear side and the acceleration phase of the ablation front do not occur at the same time. The planar foil has a lower temperature because more internal energy is converted into kinetic energy due to larger

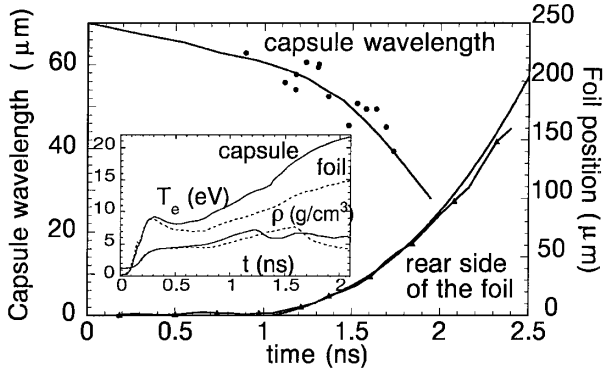

FIG. 3. Measurements of the rear side trajectory of a planar foil (triangles) and of the wavelength evolution of a capsule (circles) are compared to postprocessed simulations. In the inset the peak density and the electron temperature at the location of peak density are plotted versus time for both the planar and spherical cases.

decompression after shock breakout in planar geometry. One way to put these two configurations on more "equal footing" for comparing their RT growth is to look at the evolution of the perturbation amplitudes versus $\sqrt{s}$, where s is the distance accelerated.

Finally, we used a postprocessor code to simulate radiographs [18], taking into account the spatial and time resolution of the diagnostics. The predicted radiograph is then Fourier analyzed in the same way as the experimental images.

Measured and simulated RT growth factors for the planar foil are plotted in Fig. 4, both for the fundamental mode and its second harmonic. In Fig. 5, the same is plotted for the spherical target. The experimental results, given by the square symbols, correspond to the Fourier analysis of a 3-4 period signal. The Fourier transform is done on the ln(exposure) profile after subtracting the background from the backlighter. The experimental error bars are calculated as the average of the neighboring modes, which is a reasonable measure of the uncertainty in the analysis method. The curves labeled "radiography simulation" represent the simulated optical depth modulation versus time accounting for the experimental resolution of the diagnostics, quantified by its modulation transfer function $M(k)$. The instrument resolution has been extensively characterized [19] and is included in our analysis during postprocessing the simulations. The functional form of the modulation transfer function (MTF) used here is given by

$$M(k) = \frac{1}{1 + a}\left[\exp\left(-\frac{k^2}{2b^2}\right) + a\exp\left(-\frac{k}{c}\right)\right], \quad (1)$$

where $k = \frac{2\pi}{\lambda}$ is the mode wave number, and $(a, b, c) = (0.093, 0.24\ \mu\mathrm{m}^{-1}, 0.030\,77\ \mu\mathrm{m}^{-1})$. The curves labeled FCI2 in Figs. 4 and 5 are coefficients of the Fourier transform of the spatial amplitude extracted from the simulations, based on an isodensity contour at the perturbed ablation front. The time calibration between experiment and simulation is verified by correctly reproducing the wavelength evolution $\lambda(t)$ for the spherical case and the foil trajectory for the planar case (see Fig. 3). The shock breaks out the back (inner) side of the foil (capsule) at 1.6 ns (1.2 ns), based on the simulations and the measured foil trajectory.

A heuristic relation [20] between growth factors in optical depth (GF_τ) and in spatial amplitude (GF_z)

$$\mathrm{GF}_\tau(t) = \frac{\rho}{\rho_0}\,\mathrm{GF}_z(t) \quad (2)$$

can be applied considering a constant value for the opacity coefficient.

As the first shock propagates through the target, there is lateral flow of material from bubble to spike due to the rippled shock dynamics [21] (even in the linear regime, we use "spike" to denote the heavy material penetrating the light material and conversely for the "bubble"). This is perceived only via the optical depth GF_τ, and GF_z stays approximately flat [22].

After the shock breaks out the back side of the foil and the rarefaction wave returns to the ablation front, the foil as a whole is accelerated. Perturbations at the ablation front grow. As mass flows from bubble to spike, the density in the spike increases relative to the bubble. As the perturbation enters the nonlinear regime, as evidenced by the appearance of the second harmonic, more and more mass is contained in a narrow spike, which is not fully resolved. The apparent saturation for GF_τ seen in the radiography simulation curves in Figs. 4 and 5 results from the combined effect of the decompression, the change in the opacity coefficient depending on local density and temperature (after 1.8 ns in our spherical simulations), and the finite instrument spatial resolution. At the same time, the spatial growth factor GF_z, localized at the ablation front, departs from purely linear regime (i.e., exponential growth) but shows no evidence of saturation. In spherical geometry, two additional effects need to be considered: (i) The instrument spatial resolution, quantified in Eq. (1) by its MTF as the wavelength $\lambda = \frac{2\pi}{k}$, decreases

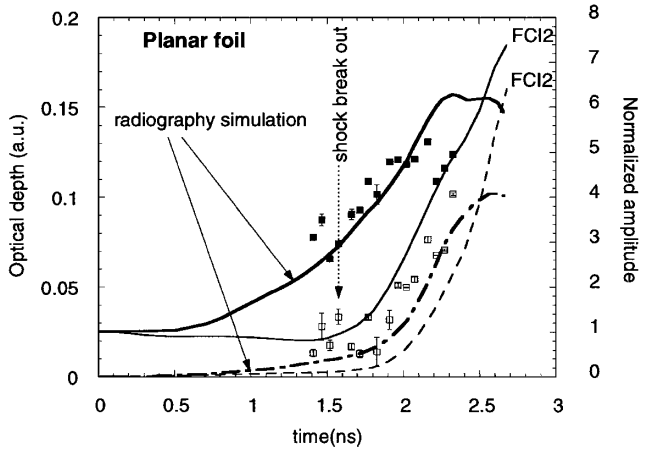

FIG. 4. Fourier analysis of the planar data compared to the postprocessed numerical results for the fundamental mode (solid curves) and its second harmonic (dashed curves).

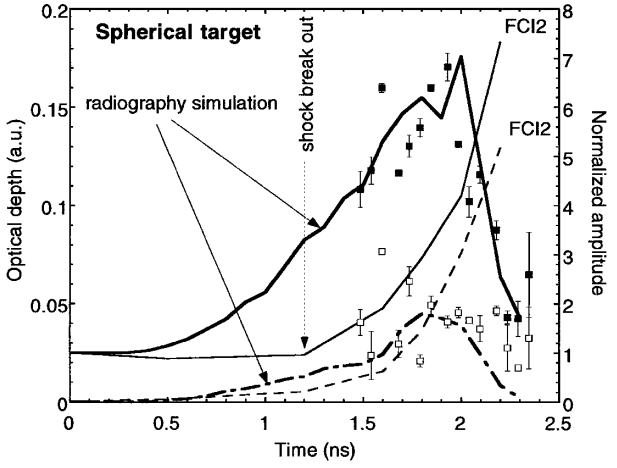

FIG. 5. Fourier analysis of the convergent data compared to the postprocessed numerical results for the fundamental mode (solid curves) and its second harmonic (dashed curves).

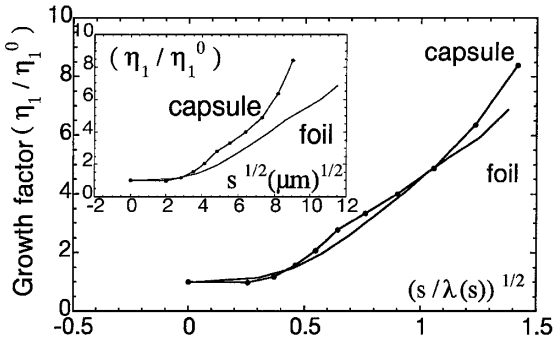

FIG. 6. Simulated $\frac{\eta_1}{\eta_1^0}$ versus $\sqrt{\frac{s}{\lambda}}$, where s is the distance accelerated, for the planar and convergent cases. For small convergence ratio, the dominant effect of convergence is the shrinking of the wavelength.

during convergence. The saturation of GF_τ is not dominated by the instrument MTF, at least for a 70 μm wavelength over a convergence ratio of 2, as verified by postprocessing the simulations with the actual instrument MTF and for a MTF corresponding to a smaller pinhole. (ii) The deviation of the spikes from the diagnostic line of sight is a concern. We notice no systematic trend in observed ripple amplitude as one moves away from the center of the image; hence we conclude that this is not a significant effect.

As mentioned above, direct comparisons of the planar and convergent cases versus time are difficult. Instead, we examine the evolution of the perturbation amplitudes versus $\sqrt{s}$, where s is the distance accelerated. As the acceleration is not really constant in these experiments, this distance will be extracted directly from the FCI2 simulations. We define s as the distance traveled by the ablation front, starting from the time t_0 when the acceleration stage begins. Using growth factors of spatial amplitude at the ablation surface, determined directly from the simulations, we show $\frac{\eta_1}{\eta_1^0}$ versus $\sqrt{s}$ in the inset in Fig. 6, where $\eta_1^0 = \eta_1(t = 0)$. In this representation, the convergent case grows more rapidly.

According to [23], the ratio of the second harmonic to fundamental mode amplitudes $\frac{\eta_2}{\eta_1}$ is a good measure of nonlinearity. From examination of $\frac{\eta_2}{\eta_1}$ (not shown), we find that the convergent case enters the nonlinear regime sooner, too. However, when $\frac{\eta_1}{\eta_1^0}$ is plotted versus $\sqrt{\frac{s}{\lambda(s)}}$ in Fig. 6, the planar and convergent cases appear nearly identical.

Hence, we conclude that for small convergence ratios and weakly nonlinear hydrodynamics, the dominant effect of convergence is simply the shrinking of the wavelength, an effect we denote as "passive convergence." This passive convergence does not alter or create new effects in the instability evolution. Once account is taken for the shrinking of the wavelength, standard weakly nonlinear hydrodynamics is followed in both cases, as long as the higher order Fourier harmonics stay small. The higher harmonics become nonnegligible in our experiment at about 1.7 ns for the capsule, and 2.0 ns for the foil, corresponding for both cases to $\sqrt{\frac{s}{\lambda(s)}}$ close to unity. Our future work will develop higher convergence ratio experiments and a longer acceleration stage to achieve more nonlinear RT to observe the transition from passive to active convergence.

The authors thank M. Bonnefille, L. Hallo, P. A. Holstein, G. Schurtz, and S. Weber for helpful discussions, and the highly skilled staff of Nova. This work has been performed under the auspices of a "Commissariat à l'Energie Atomique/U.S. Department of Energy" collaboration.

[1] A. J. Cole *et al.,* Nature (London) **299**, 329 (1982).
[2] J. Grun *et al.,* Phys. Rev. Lett. **58**, 2672 (1987).
[3] M. Desselberger *et al.,* Phys. Rev. Lett. **65**, 2997 (1990).
[4] S. G. Glendinning *et al.,* Phys. Rev. Lett. **69**, 1201 (1992).
[5] B. A. Remington *et al.,* Phys. Fluids B **4**, 967 (1992); **5**, 2589 (1993).
[6] J. S. Wark *et al.,* Appl. Phys. Lett. **48**, 969 (1986).
[7] H. Nishimura *et al.,* Phys. Fluids **31**, 2875 (1988).
[8] W. W. Hsing and N. M. Hoffmann, Phys. Rev. Lett. **78**, 3876 (1997); W. Hsing *et al.,* Phys. Plasmas **4**, 1832 (1997).
[9] S. T. Weir *et al.,* Phys. Rev. Lett. **80**, 3763 (1998).
[10] S. G. Glendinning *et al.,* Bull. Am. Phys. Soc. **41**, 1526 (1996).
[11] S. G. Glendinning *et al.,* in *Proceedings of the 6th International Workshop on the Physics of Compressible Turbulent Mixing, 1997,* edited by G. Jourdan and L. Houas (Imprimerie Caractère, Marseille, France, 1997), p. 173.
[12] C. Cherfils *et al.,* in *Proceedings of the 6th International Workshop on the Physics of Compressible Turbulent Mixing, 1997* (Ref. [11]), p. 116.
[13] O. L. Landen *et al.,* Phys. Plasmas **3**, 2094 (1996).
[14] R. J. Wallace *et al.,* Inertial Confinement Fusion Quarterly Report No. UCRL-LR-105821-94-3, 1994.
[15] B. K. Bradley *et al.,* Rev. Sci. Instrum. **66**, 716 (1995).
[16] G. Schurtz, in *La Fusion Thermonucleaire Inertielle par Laser,* edited by R. Dautray *et al. (*Eyrolles, Paris, France, 1994), Vol. 2, pp. 1055–1226; M. Busquet, Phys. Fluids B **5**, 4191 (1998); E. Buresi *et al.,* Laser Part. Beams **4**, 531 (1986).
[17] S. Laffite, CEA Internal Report (unpublished). See also Fig. 5 in S. V. Weber *et al.,* Phys. Plasmas **5**, 2988 (1988) for the case of a similar preformed Nova pulse.
[18] P. Humbert, in *Abstracts of the Europhysics Conference on Plasma Physics, Innsbruck, 1992* (European Physical Society, Frankfurt, 1992), Vol. 16C, p. 1249.
[19] S. G. Glendinning *et al.,* Phys. Rev. E **54**, 4473 (1996), Fig. 3(a); M. M. Marinak *et al.,* Phys. Rev. Lett. **75**, 3677 (1995); M. F. Robey *et al.,* Rev. Sci. Instrum. **68**, 792 (1997).
[20] S. G. Glendinning *et al.,* Phys. Rev. Lett. **78**, 3318 (1997).
[21] T. Endo *et al.,* Phys. Rev. Lett. **74**, 3608 (1995).
[22] V. N. Goncharov, Phys. Rev. Lett. **82**, 2091 (1999).
[23] S. A. Bel'kov *et al.,* Phys. Plasmas **5**, 2988 (1998).